

Differential conductance and noise spectrum in a quantum dot coupled to a superconducting nanowire

Huajin Zhao, Junrong Wang, Hong Mao,* and Jinshuang Jin†
School of Physics, Hangzhou Normal University, Hangzhou, Zhejiang 311121, China
(Dated: May 24, 2024)

We investigate the quantum transport through a quantum dot coupled with a superconducting (SC) nanowire. The distinguishing characteristics between the Majorana bound states (MBSs) and Andreev bound states (ABSs) hosted in SC wire are demonstrated in the differential conductance and finite-frequency current noise spectrum. The former shows the well-known zero-bias peak (ZBP), while the latter displays the degenerate Rabi dip (DRD) for MBSs with topological quality factor $q = 1$. However, for ABSs with $q < 1$, the ZBP and DRD split. We confirm that the ABSs with high quality factors greater than critical values can mimic the signatures of topological MBSs. Especially, the corresponding critical quality factors for the occurrence of ZBP and DRD are explicitly obtained and their underlying mechanisms are addressed.

PACS numbers: 73.63-b, 05.40.Ca, 05.60.Gg

I. INTRODUCTION

Stimulated by the potential applications in topological quantum computations [1–4], Majorana bound states (MBSs) have attracted extensive attention in both theoretical [5–12] and experimental studies [13–17]. In practice, several realizations of the physical Majorana platforms have been proposed in Refs.[5–12]. Among these studies, the spin-orbit coupling semiconductor nanowires proximity coupled to a superconductor is the popular realization scheme, where the zero energy MBSs are expected to host at the end of the nanowires [5, 6]. The experiments aim to verify the presence of MBSs, but the evidence of MBSs is still under debate. Although the transport measurement for the tunneling spectroscopy has been studied in either single-lead (two-terminal) setups [7–10], or two-lead (three-terminal) setups [11, 12]. The observation of both the zero-bias conductance peak and its quantized value $2e^2/h$ are not the sufficient condition for identifying the existence of MBSs [18–22]. Therefore, it is believed that a more powerful proposal for inferring Majorana signatures is to detect nonlocality, such as quantum correlation [23–33] or interferometry [34, 35]. For example, the hybrid setup of the MBSs are coupled to two quantum dots have been suggested in Refs.[26–33]. However, how to realize those schemes remain a great challenge to the current experiments. So that an alternative scheme which is more realizable is still in demand.

Recently, it has been proposed that the nonlocal behavior of a topological system may be tested through a local measurement with the aid of a quantum dot (QD) at the wires’s end [36, 37], as illustrated in Fig. 1. For instance, the Majorana non-locality was characterized by a “topological quality factor q ”, which is defined as [36] $q = 1 - \lambda_2/\lambda_1$. Here, λ_1 and λ_2 are the couplings be-

tween the two Majorana modes and the QD. The topological quality factor q could be obtained from differential conductance measurements through the QD, which has been experimentally implemented in Ref. [38]. The observed zero-bias conductance peak corresponds to highly quality factor $q \rightarrow 1$ when the SC wire hosts purely topological MBSs and its splitting corresponds to $q < 1$ when the SC wire hosts trivial Andreev bound states (ABSs). Soon afterwards, it has been demonstrated that the ABSs with partially separated Majorana states, which is the so-called quasi-MBSs (for short, qMBSs) with $\lambda_2 \ll \lambda_1$, can also give rise to high quality factors. Hence, the qMBSs subsequently mimic the signatures of spatially separated topological MBSs [39, 40]. This makes the Majorana non-local nature unsuitable for distinguishing between qMBSs and topological MBSs by the local measurement as proposed in Refs [36, 37]. Therefore, there exist two basic questions which should be resolved as follows. One is that how high is the quality factor (its critical value) of qMBSs to mimic the characteristics of MBSs. The other is what the physical mechanism determines the critical value of the quality factor. We believe that studies related to these two special issues will be helpful for the current experimental demonstrations.

In this paper, we will thoroughly study the quantum transport through a QD coupled with a superconducting (SC) nanowire. In terms of the differential conductance and the finite-frequency current noise spectrum, we firstly demonstrate the distinguishing characteristics between topological MBSs and trivial ABSs hosted in the SC wire. Then, the qMBSs with high quality factors larger than the critical values are exhibited to mimic the signatures of spatially separated topological MBSs. More importantly, we also reveal the underlying mechanism governing the critical values of the quality factors for the emergence of ZBP in the differential conductance and DRD in the noise spectrum, respectively. At last, the quantitative expressions for the critical quality factors are provided and they could be useful for the current experimental demonstrations.

*Electronic address: mao@hznu.edu.cn

†Electronic address: jsjin@hznu.edu.cn

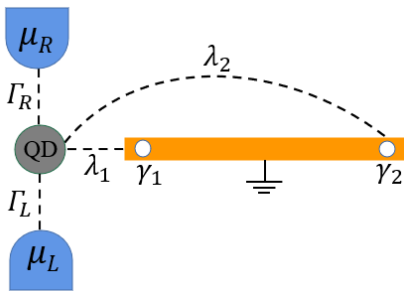


FIG. 1: (Color online) Schematic diagram for the transport through the QD-wire hybrid system. The QD is contacted by the two electron reservoirs under the bias voltage ($V = \mu_L - \mu_R$) and laterally coupled to the two Majorana modes (γ_1 and γ_2). They are hosted in the superconducting wire with the coupling coefficients λ_1 and λ_2 , respectively.

The remainder of this paper is organized as follows. In Sec. II, we introduce the hybrid transport model and the employed quantum master equation approach. The related superoperators involved in current expression and the noise formula are defined in Appendix A. We present the results in Sec. III. First, we analyze the QD-wire Hamiltonian eigenspectrum in Sec. III A together with Appendix B. Then we demonstrate the detail results for the differential conductance and the current noise spectrum in Sec. III B and Sec. III C, respectively. Finally, we give the summary in Sec. IV.

II. METHODOLOGY

A. Model description

We consider the electron transport through a quantum dot (QD) which is laterally coupled to a superconducting (SC) nanowire as schematically shown in Fig. 1. The composed Hamiltonian consists of three parts, $H_{\text{tot}} = H_B + H' + H_S$. The first part is the bath Hamiltonian of the two electron reservoirs which is given by $H_B = \sum_{\alpha} (\varepsilon_{\alpha k} + \mu_{\alpha}) \hat{c}_{\alpha k}^{\dagger} \hat{c}_{\alpha k}$, with the applied bias voltage $V = \mu_L - \mu_R$. The second part is the coupling Hamiltonian between the reservoirs and QD. It is described by the standard tunneling form,

$$H' = \sum_{\alpha=L,R} \hat{F}_{\alpha}^{\dagger} \hat{d} + \hat{d}^{\dagger} \hat{F}_{\alpha}, \quad (1)$$

where \hat{d}^{\dagger} (\hat{d}) is the electron creation (annihilation) operator in the QD with the assumption of a single fermionic mode, and $\hat{F}_{\alpha}^{\dagger} \equiv \sum_k t_{\alpha k} \hat{c}_{\alpha k}^{\dagger}$ with the tunneling coefficients $t_{\alpha k}$ and $\alpha = L, R$. Throughout this work, we adopt units of $e = \hbar = 1$ for the electron charge and the Planck constant.

The primary interest is the QD-wire hybrid system in the third part of the composed Hamiltonian. It can be

simply described by the low energy Hamiltonian [36],

$$H_S = \varepsilon_D \hat{d}^{\dagger} \hat{d} + i\varepsilon_M \gamma_1 \gamma_2 + (\lambda_1 \hat{d}^{\dagger} \gamma_1 + i\lambda_2 \hat{d}^{\dagger} \gamma_2 + \text{H.c.}). \quad (2)$$

Here, the first term is the Hamiltonian of the QD with the energy level ε_D . The wire hosts a pair of Majorana modes γ_1 and γ_2 with the coupling energy ε_M . The last term in Eq. (2) describes the coupling between the dot and two Majorana modes with the two different coupling coefficients λ_1 and λ_2 , which are assumed to be positive real. If the wire is in the topological regime, λ_2 should be zero ($\lambda_2 \rightarrow 0$). It corresponds to that there are two MBSs with the modes γ_1 and γ_2 located at the two ends of the wire. Otherwise ($\lambda_2 \neq 0$), the wire is in the non-topological regime where the mode γ_2 is close to mode γ_1 . In this case, the wire bears trivial ABSs including quasi-MBSs (qMBSs) as γ_1 and γ_2 are partially separated with $\lambda_2 \ll \lambda_1$ [39–42].

For convenience, in what follows, we introduce a ratio parameter $\xi \equiv \frac{\lambda_2}{\lambda_1}$, which is related to the quality factor $q = 1 - \xi$ as defined in Ref. 36. That is, $\xi = 0$ ($q = 1$) and $\xi > 0$ ($q < 1$) correspond to the topological MBSs and trivial ABSs hosted in the SC wire, respectively. Furthermore, for the case of $\xi = 1$ ($q = 0$), γ_1 and γ_2 combine to form a local regular fermion. This leads to the disappearance of Andreev process in the dot-wire Hamiltonian of Eq. (2), as demonstrated explicitly in Eq. (B1) in Appendix B. In this work, our study will focus on the different characteristics of the differential conductance and current fluctuation spectrum between MBSs and ABSs hosted in SC wire. In particular, we will explore the dependence of these transport characteristics on the parameter ξ (or the quality factor q).

B. Quantum master equation approach

For the consideration of the weak QD-reservoir coupling [c.f. Eq. (1)], we apply the second-order quantum master equation (QME) with memory effect. It is described by the time-nonlocal QME [43–46],

$$\dot{\rho}(t) = -i\mathcal{L}_S \rho(t) - \sum_{\alpha\sigma} \int_{t_0}^t d\tau [\hat{d}^{\sigma}, \mathcal{C}_{\alpha}^{(\sigma)}(\mathcal{L}_S, t - \tau) \rho(\tau)], \quad (3)$$

where $\mathcal{L}_S \bullet = [H_S, \bullet]$, $\sigma = \pm$ with $\hat{d}^+ \equiv \hat{d}^{\dagger}$ ($\hat{d}^- \equiv \hat{d}$) and

$$\mathcal{C}_{\alpha}^{(\sigma)}(\mathcal{L}_S, t) \bullet \equiv e^{-i\mathcal{L}_S(t-\tau)} [c_{\alpha}^{(\sigma)}(t) \hat{d}^{\sigma} \bullet - c_{\alpha}^{(\bar{\sigma})*}(t) \bullet \hat{d}^{\sigma}]. \quad (4)$$

The bath correlator is defined by $c_{\alpha}^{(\sigma)}(t - \tau) = \langle \hat{F}_{\alpha}^{\sigma}(t) \hat{F}_{\alpha}^{\bar{\sigma}}(\tau) \rangle$. In Eq. (3), the first term describes the intrinsic coherent dynamics of the dot-wire hybrid system. The second term represented by the convolution of the time depicts the non-Markovian dissipative effect of the coupled electron reservoirs.

The current through the system via the definition of $I_{\alpha}(t) = -\frac{\langle d\hat{N}_{\alpha}(t) \rangle}{dt}$ with $\hat{N}_{\alpha} \equiv \sum_k \hat{c}_{\alpha k}^{\dagger} \hat{c}_{\alpha k}$, is given by

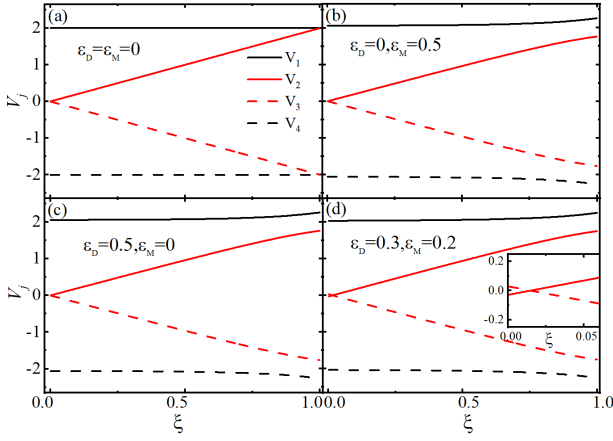


FIG. 2: (Color online) Low-energy spectrum characterizing the conductance peak positions (V_j) as a function of ξ . The results of the cases of $\varepsilon_D = 0$ or $\varepsilon_M = 0$ are shown in (a)-(c), where the ZBP occurs at $V_2 = V_3 = 0$ for $\xi = 0$ and splits for $\xi \neq 0$. The result of both finite value of ε_D and ε_M is shown in (d), where the ZBP emerges for $\xi \neq 0$ as enlarged in the inset.

[43, 47, 48]

$$I_\alpha(t) = -\sum_{\sigma u} \int_{t_0}^t d\tau \text{tr}_s[\tilde{d}^\sigma \mathcal{C}_\alpha^{(\bar{\sigma})}(\mathcal{L}_s, t - \tau)\rho(\tau)], \quad (5)$$

where $\tilde{d}^\sigma \equiv \sigma \hat{d}^\sigma$. The stationary current can be further expressed with $\bar{I}_\alpha = [\mathcal{J}_\alpha^>(0)\bar{\rho}] = \text{tr}_s[\mathcal{J}_\alpha^<(0)\bar{\rho}]$. Here, the superoperators $\mathcal{J}_\alpha^{>,<}$ are defined in Eq. (A1a). $\bar{\rho}$ is the steady state of the dot-wire hybrid system which is the solution of $\dot{\rho}(t) = 0$ in Eq. (3).

The current noise spectrum, i.e., $S_{\alpha\alpha'}(\omega) = \int_{-\infty}^{\infty} dt e^{i\omega t} \langle \delta \hat{I}_\alpha(t) \delta \hat{I}_{\alpha'}(0) \rangle$ with $\delta \hat{I}_\alpha(t) \equiv \hat{I}_\alpha(t) - \bar{I}_\alpha$, can be calculated via the formula [48]

$$S_{\alpha\alpha'}(\omega) = 2\delta_{\alpha'\alpha} \text{Re} \sum_{\sigma} \text{tr}_s[\hat{d}^\sigma c_\alpha^\sigma(\omega - \mathcal{L}_s)(\hat{d}^\sigma \bar{\rho})] + \text{tr}_s \left\{ \mathcal{J}_{\alpha'}^<(-\omega) \mathcal{G}(-\omega) [\mathcal{J}_\alpha^<(0) + \mathcal{W}_\alpha^<(-\omega)] \bar{\rho} + \mathcal{J}_\alpha^>(\omega) \mathcal{G}(\omega) [\mathcal{J}_{\alpha'}^>(0) + \mathcal{W}_{\alpha'}^>(\omega)] \bar{\rho} \right\}, \quad (6)$$

where the related superoperators are defined in the Appendix A. The asymmetrical quantum noise spectrum in Eq. (6) can be used to describe energy absorption with $\omega > 0$ and energy emission with $\omega < 0$ processes, simultaneously [49–51].

III. RESULTS

A. Hamiltonian eigenspectrum

In order to illustrate the results of the differential conductance and current noise spectrum, we first briefly analyze the Hamiltonian eigenspectrum of the QD-wire hybrid system. By substituting the Majorana modes with

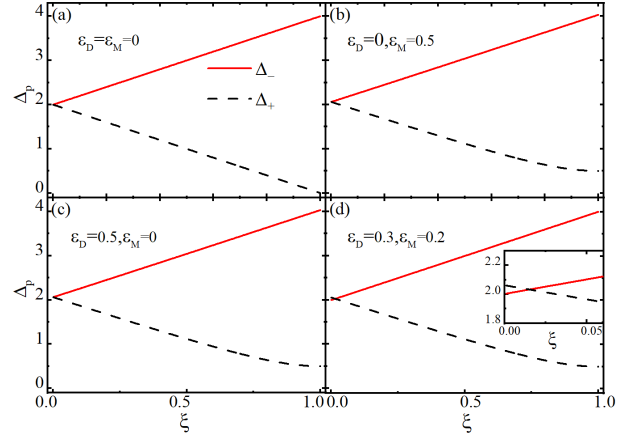


FIG. 3: (Color online) The parity-dependent Rabi frequency (Δ_p) as a function of ξ . The results of the cases of $\varepsilon_D = 0$ or $\varepsilon_M = 0$ are shown in (a)-(c). They display $\Delta_- = \Delta_+$ for $\xi = 0$ and $\Delta_- \neq \Delta_+$ for $\xi \neq 0$. The result of both finite value of ε_D and ε_M is shown in (d). It displays $\Delta_- = \Delta_+ \xi \neq 0$ as enlarged in the inset.

the regular fermion, i.e., $\gamma_1 = f + f^\dagger$ and $\gamma_2 = -i(f - f^\dagger)$, the Hamiltonian of the QD-wire hybrid system [Eq. (2)] can be rewritten as the summation of the normal tunneling and Andreev reflection processes. These two processes induce the intrinsic Rabi oscillations in both odd-parity ($p = -1$) and even-parity ($p = +1$) subspaces. Then, the corresponding parity-dependent Rabi frequency reads

$$\Delta_p = \sqrt{(\varepsilon_D + p\varepsilon_M)^2 + 4(\lambda_1 - p\lambda_2)^2}. \quad (7)$$

Usually, the finite-frequency noise spectrum exhibits some obvious characteristics at Rabi frequency Δ_p . For instance, it has been demonstrated that a dip feature occurs at Rabi frequency in the noise spectrum in both serial and parallel coherent coupled double dots [47, 52–54]. Hence, we could expect that the feature of the parity-dependent Rabi signal at $\omega \simeq \pm \Delta_p$ should emerge in the finite-frequency current noise spectrum.

On the other hand, the conductance peaks appear whenever the Fermi surface of the electrode is on resonance with the allowed transitions between the ground state and an excited state with the opposite parity. The resulting peak positions are expressed in descending order as

$$V_1 = \frac{1}{2}(\Delta_+ + \Delta_-), \quad V_2 = \frac{1}{2}(-\Delta_+ + \Delta_-), \\ V_3 = \frac{1}{2}(\Delta_+ - \Delta_-), \quad V_4 = -\frac{1}{2}(\Delta_+ + \Delta_-). \quad (8)$$

Here, we leave the detail analysis of the Hamiltonian eigenspectrum in Appendix B for consultation. From Eqs. (7) and (8), it is easy to find that the zero-bias peak (ZBP) develops at $V_2 = V_3 = 0$ when $\Delta_+ = \Delta_-$ under the condition,

$$\varepsilon_D \varepsilon_M = 4\lambda_1 \lambda_2 = 4\xi \lambda^2, \quad (9)$$

where we defined $\lambda_1 = \lambda$ and $\lambda_2 = \xi\lambda$ with $0 \leq \xi < 1$.

For $\xi = 0$, the wire hosts a pair of nonlocal MBSs at the two ends and is in the perfect topological system. This suggests that the dot is only coupled to the nearby Majorana mode γ_1 whereas the coupling coefficient λ_2 vanishes. Furthermore, from Eq. (9), we have the cases of $\varepsilon_D = 0$ or $\varepsilon_M = 0$. For each situation, the ZBP can be produced and the Rabi features at Δ_+ and Δ_- in the noise spectrum will become degenerate due to $\Delta_+ = \Delta_-$. However, when $\xi \neq 0$ ($0 < \xi < 1$), the dot is coupled to the two Majorana modes γ_1 and γ_2 simultaneously. Then, the wire is in the nontopological regime and hosts trivial ABSs. Consequently, in the cases of $\varepsilon_D = 0$ or $\varepsilon_M = 0$, both the ZBP in the conductance and the degenerate Rabi signal in the noise spectrum become split as displayed in Fig. 2(a)-(c) and Fig. 3(a)-(c). Considering a local regular fermion in the wire with $\xi = 1$, the conductance displays two peaks at $V_1 = V_2$ and $V_3 = V_4$ for $\varepsilon_M = \varepsilon_D = 0$. Whereas it exhibits four peaks for either $\varepsilon_M \neq 0$ or $\varepsilon_D \neq 0$ since $V_1 \neq V_2$ and $V_3 \neq V_4$. Meanwhile, the noise spectrum only illustrates the Rabi signal of Δ_- , as the Rabi oscillation in even parity space no longer exists [c.f. Eq. (B1)].

It is worth noting that the ZBP can also be developed and the two Rabi signal are degenerate even for $\xi \neq 0$ as long as $\varepsilon_D \neq 0$ and $\varepsilon_M \neq 0$ as inferred from Eq. (9). We demonstrate these numerical illustrations in Fig. 2(d) and Fig. 3(d), and also Fig. 7 and Fig. 8 in the Appendix B. In order to study the distinguishing characteristics between the topological MBSs and trivial ABSs, our study mainly focus on the cases of $\varepsilon_D = 0$ or $\varepsilon_M = 0$ in what follows.

From the above Hamiltonian, it seems that either the ZBP in the conductance or the degenerate Rabi signal in the noise spectrum can be taken as a hallmark for the existence of MBSs ($\xi = 0$) in SC wire. However, for the realistic measurement setup, such a conclusion is not actually exact as shown in Fig. 1, where the dot is contacted by the two electrodes. Now, the electrodes are regarded as environments and induce the dissipative effect on the QD-wire hybrid system. We will analyse this problem in the following sections.

B. The differential conductance

Let us demonstrate the characteristics of differential conductance in the transport measurement setup of Fig. 1. In calculations, we consider the symmetrical-lead situation, where $\mu_L = -\mu_R = V/2$ and $\Gamma_L = \Gamma_R = \Gamma/2$. Then, we have $G = G_L = -G_R = \frac{dI}{dV}$. Furthermore, we set $\lambda = 1$ as a unit of the energy level and consider wide bandwidth limit $W \gg \Gamma$ for the electron reservoirs. The parameters of the coupling strength Γ and the electrode temperature $k_B T$ are adopted in the weak coupling regime with $\Gamma \lesssim k_B T$.

Figure 4 depicts the characteristics of differential conductance as a function of the bias voltage, in which the conductance peaks occur at $|\mu_\alpha| = V/2 = V_i$, ($i =$

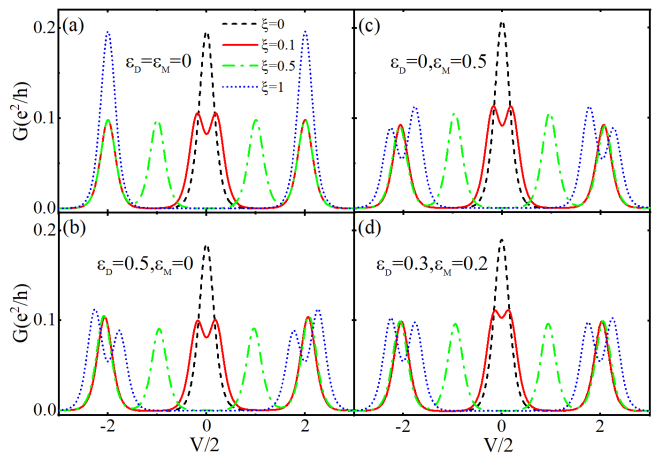


FIG. 4: (Color online) The differential conductance G as a function of bias voltage V with different ξ . The results are shown in (a) $\varepsilon_D = \varepsilon_M = 0$, (b) $\varepsilon_D = 0, \varepsilon_M = 0.5$, (c) $\varepsilon_D = 0.5, \varepsilon_M = 0$, and (d) $\varepsilon_D = 0.3, \varepsilon_M = 0.2$. The other parameters are $k_B T = 0.1$ and $\Gamma = 0.1$.

1, 2, 3, 4). As the results shown in Fig. 4(a)-(c), the conductance features are consistent with those demonstrations in Fig. 2(a)-(c). The conductance indeed displays three peaks for $\xi = 0$ (MBSs). The height of ZBP is twice than that of the other two peaks due to the coincidence of two peaks ($V_2 = V_3 = 0$) at zero-bias voltage. For the wire bearing ABSs with $0 < \xi < 1$, the ZBP splits ($V_2 \neq V_3 \neq 0$) and it leads to four peaks. For the regular local fermion with $\xi = 1$, two peaks appear with the same heights as the ZBP when $\varepsilon_M = \varepsilon_D = 0$ (see Fig. 2(a)). This is induced by the degenerate of the peaks at V_1, V_2, V_3 and V_4 with $V_1 = V_2$ and $V_3 = V_4$. On the contrary, for either the case of $\varepsilon_D \neq 0$ or the case of $\varepsilon_M \neq 0$, the degenerate peaks are split and there have four peaks as displayed in Fig. 4(b) and Fig. 4(c). Furthermore, the heights of four peaks in Fig. 4(b) and Fig. 4(c) are different, due to the nonsymmetric tunneling channels with $\varepsilon_M \neq \varepsilon_D$.

Note that the conductance characteristic in Fig. 4(d) for both small values of ε_M and ε_D also exhibit the ZBP for $\xi = 0$. This feature is different from that illustrated in Fig. 2(d), where the ZBP emerges at $\xi = 0.015$ according to Eq. (9). The reason is that the contacted electron reservoirs induce dissipative effect on the QD-wire system, and the resulting conductance has certain broadening as illustrated in Fig. 4. We find that the broadening is dominated by the temperature for the weak coupling regime ($\Gamma \lesssim k_B T$). To illustrate this point, we provide an analytical expression by using $\varepsilon_D = \varepsilon_M = 0$ as an example. The resulted differential conductance is obtained as

$$G = \frac{\Gamma\beta}{4^3} \left(\text{Sech}^2[\beta(V/4 - \lambda_1)] + \text{Sech}^2[(V/4 + \lambda_1)] + \text{Sech}^2[\beta(V/4 - \lambda_2)] + \text{Sech}^2[\beta(V/4 + \lambda_2)] \right), \quad (10)$$

where we have considered the symmetrical-lead situa-

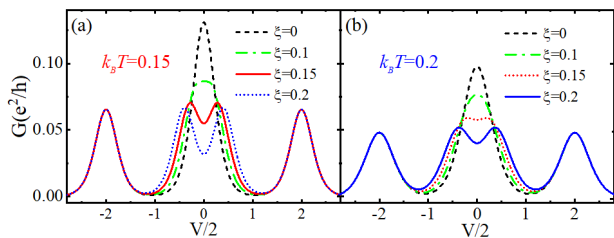


FIG. 5: (Color online) The differential conductance G as a function of bias voltage V with different ξ , for (a) $k_B T = 0.15$ and (b) $k_B T = 0.2$. The other parameters are $\varepsilon_D = \varepsilon_M = 0$ and $\Gamma = 0.1$.

tion as mentioned above. Evidently, the conductance described by Eq. (10) indicates that the peaks arise at the bias voltage of $V/2 = V_1 = 2\lambda_1 = -V_3$ and $V/2 = V_2 = 2\lambda_2 = -V_4$, which are consistent with those given by Eq. (8). Moreover, the profile of the conductance is determined by the temperature, while the height is dominated by both the coupling strength and temperature.

From Fig. 4 and Fig. 2, it is found that the key to distinguish ABSs from MBSs based on the conductance characteristics is to observe whether the ZBP splits or not. However, the feature of Fig. 4(d) suggests that we actually cannot discern between the characteristics of $\xi = 0$ (MBSs) and $\xi = 0.015$ (qMBSs) (even $\xi < 0.1$) due to the broadening effect. That is, the temperature-induced broadening effect of the conductance exactly limits the efficiency for the distinction between MBSs and ABSs. Therefore, we further plot the differential conductance at different temperature in Fig. 5. It exhibits that the critical value of ZBP splitting occurs roughly at $\xi = \xi_c \approx k_B T / \lambda$. So that, we obtain the critical value of quality factor as

$$q_c = 1 - \xi_c \approx 1 - k_B T / \lambda, \quad (11)$$

which is applicable for $\varepsilon_M = 0$ or $\varepsilon_D = 0$, even for very small values of $\varepsilon_M, \varepsilon_D \ll \lambda$. Moreover when considering the actual situation in experiments, it is better to tune the energy level of the dot as $\varepsilon_D \rightarrow 0$, since the coupling energy (ε_M) of Majorana modes is determined by the length of the wire.

Note that the critical quality factor given by Eq. (11) can also be referred to as the discrimination efficiency between topological MBSs and trivial ABSs, i.e., $\eta_c = q_c$. Apparently, η_c cannot reach 1 for the finite temperature. We can only distinguish the conductance features between $q > q_c$ and $q \lesssim q_c$. Here, the former case ($q > q_c$) displays ZBP and the latter case ($q \lesssim q_c$) is exactly ZBP splitting. Such a result could be used to explain the fact that the partially separated of qMBSs with high quality factor ($q > q_c$ with $\lambda_2 \ll \lambda_1$) mimic the characteristics of MBSs ($q = 1$), and thus cannot be distinguished from the spatially separated topological MBSs, as exhibited in the previous works [39, 40].

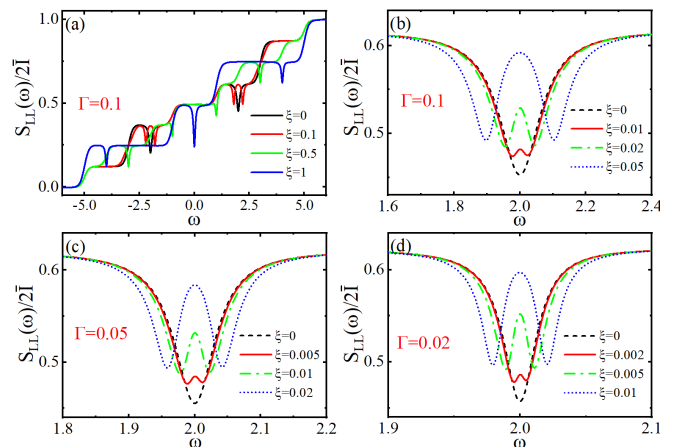


FIG. 6: (Color online) The auto-correlation current noise spectrum of the left-lead, $S_{LL}(\omega)$, with different ξ . The results are shown in (a) and (b) $\Gamma = 0.1$, (c) $\Gamma = 0.05$, and (d) $\Gamma = 0.02$. The other parameters are $\varepsilon_M = \varepsilon_D = 0$, $k_B T = 0.1$, and $V = 8$.

C. Noise spectrum

We are now in the position to demonstrate the finite-frequency current noise spectrum which contains the information beyond the conductance as well-known. Actually, the above illustrated feature of the differential conductance reflects the energy transition (structure) information of the QD-wire system. While the current noise spectrum is related to not only the energy transitions but also the intrinsic coherent dynamics of the system. For the case of energy transitions, it is manifested as the non-Markovian quasi-steps at resonance frequencies, $\pm|\mu_\alpha - V_i|$, as displayed in Fig. 6 (a). This feature arises from the non-Markovian dynamics of the electrons in α -electrode tunneling into and out of the system, accompanied by energy absorption ($\omega > 0$) and emission ($\omega < 0$), respectively. The corresponding differential characteristics ($\frac{dS_{LL}(\omega)}{d\omega}$), in which the non-Markovian quasi-steps become peaks at $\pm|\mu_\alpha - V_i|$, are similar to those of the differential conductance as illustrated above.

Furthermore, of particular interest is the characteristic of the intrinsic coherent dynamics in the noise spectrum, which displays the coherent Rabi signal for the emergence of the dip at $\omega \approx \pm\Delta_p$. This feature actually comes from the propagator $\mathcal{G}(\omega)$ [c.f. Eq. (A2)] in the second and third terms of Eq. (6). Note that akin to the conductance, the feature of the noise spectrum is similar for $\varepsilon_M = 0$ or $\varepsilon_D = 0$. Without loss of generality, we take $\varepsilon_M = \varepsilon_D = 0$ as an example in the following discussions.

As depicted in Fig. 6 (a), $S_{LL}(\omega)$ displays one degenerate Rabi dip (DRD) around Rabi-frequency $\Delta_+ = \Delta_-$ for $\xi = 0$ (MBSs). The DRD is separated into two dips at Δ_+ and Δ_- ($\Delta_+ \neq \Delta_-$) for $0 < \xi < 1$ (ABSs). This feature is in agreement with the illustrations in Fig. 3. When $\xi = 1$, the Rabi signal at Δ_+ vanishes for the disappearance of the Andreev reflection processes (see the

third term in Eq.(B1)). The resulting noise spectrum displays only one dip at $\Delta_- = 2\sqrt{2}\lambda$ in the high frequency regime.

Therefore, the crux of the distinction between ABSs and MBSs in the noise spectrum is to observe whether the Rabi dip splits or not. Similar to the ZBP, we find that the Rabi dip has certain broadening. It should also limit the efficiency for distinguishing between MBSs and ABSs. Unlike the conductance, the broadening effect of the Rabi dip in the noise spectrum is found to be determined by the coupling strength (Γ) rather than the temperature ($k_B T$). Moreover, we roughly get a critical value of $\xi = \xi_s \approx 0.2\Gamma/\lambda$ for the Rabi dip splitting, as illustrated in Fig.6 (b)-(d). Here, we plot the absorption noise for $\omega > 0$ only, since the same feature can be applied in the emission part for $\omega < 0$. Thus, the corresponding critical value of quality factor is

$$q_s = 1 - \xi_s = 1 - 0.2\Gamma/\lambda, \quad (12)$$

which can also be referred to as the discrimination efficiency, i.e., $\eta_s = q_s$, between topological MBSs and trivial ABSs in the noise spectrum. Apparently, the perfect efficiency cannot be reached in experiments for the finite coupling strength in the measurements. Hence, we can only distinguish the features in the noise spectrum between $q > q_s$ and $q \lesssim q_s$. The former case ($q > q_s$) displays DRD and the latter case ($q \lesssim q_s$) is exactly DRD splitting. Comparing Eq.(11) with Eq.(12), we find the relation of $q_s > q_c$ ($\eta_s > \eta_c$) for the present studied weak coupling regime $\Gamma \lesssim k_B T$. This suggests that the DRD signal of the noise spectrum is more sensitive to the trivial ABSs than the ZBP of the conductance.

IV. SUMMARY

In summary, we have thoroughly studied the differential conductance and the noise spectrum of the transport current through the quantum dot coupled with a SC wire. The study is based on the quantum master equation approach for weak system-reservoir coupling ($\Gamma \lesssim k_B T$) regime. We focus on the distinguishing characteristics of the nonequilibrium transport between the topological MBSs and trival ABSs hosted in the SC wire.

For the SC nanowire hosting topological MBSs with the topological quality factor $q = 1$, it produces not only the zero-bias peak (ZBP) in the differential conductance, but also the degenerate Rabi dip (DRD) in the noise spectrum. Both ZBP and DRD split for the SC nanowire bears ABSs with $q < 1$. However, we found that the quasi-MBSs with high quality factor ($q \rightarrow 1$) can mimic the signatures of spatially separated topological MBSs ($q = 1$). We then explored that the underlying physical mechanism is due to the dissipative effect induced by the contacted electrodes.

Moreover, we provide the quantitative expressions of the critical quality factors, q_c and q_s , for the emergence

of ZBP in the conductance and DRD in the noise spectrum, respectively. That is, we can only distinguish the transport features between $q > q_{c/s}$ and $q \lesssim q_{c/s}$. Consequently, neither ZBP nor DRD is the hallmark of MBSs in the SC wire. However, either ZBP splitting or DRD splitting is the evidence for the SC wire bearing trivial ABSs. Particularly, the DRD in the noise spectrum is more sensitive to the ABSs than the ZBP in the conductance. We expect our findings to be enlightening for current experimental demonstrations.

Acknowledgments

We acknowledge helpful discussions Prof. YiJing Yan. The support from the Natural Science Foundation of China (Grant No. 12175052) is acknowledged.

Appendix A: Superoperators in the noise spectrum formula

The detail derivation for the noise spectrum formula Eq.(6) can refer to Ref. 48. The involved superoperators in Eq.(6) read,

$$\mathcal{J}_\alpha^>(\omega)\hat{O} \equiv -\sum_\sigma \tilde{d}^{\bar{\sigma}} [c_\alpha^{(\sigma)}(\omega - \mathcal{L}_s)\hat{O}], \quad (A1a)$$

$$\mathcal{J}_\alpha^<(\omega)\hat{O} \equiv -\sum_\sigma [c_\alpha^{(\sigma)}(\omega - \mathcal{L}_s)\hat{O}]\tilde{d}^{\bar{\sigma}}, \quad (A1b)$$

$$\mathcal{W}_\alpha^>(\omega)\hat{O} \equiv \sum_\sigma [\tilde{d}^{\bar{\sigma}}, c_\alpha^{(\sigma)}(\omega - \mathcal{L}_s)(\hat{d}^\sigma \hat{O})], \quad (A1c)$$

$$\mathcal{W}_\alpha^<(\omega)\hat{O} \equiv \sum_\sigma [\tilde{d}^{\bar{\sigma}}, c_\alpha^{\bar{\sigma}*}(\mathcal{L}_s - \omega)(\hat{O}\hat{d}^\sigma)], \quad (A1d)$$

and the propagator is given by

$$\mathcal{G}(\omega) = [i(\mathcal{L}_s - \omega) + \Sigma(\omega)]^{-1}, \quad (A2)$$

with

$$\Sigma(\omega)\hat{O} = \sum_{\alpha\sigma} [\hat{d}^{\bar{\sigma}}, c_\alpha^{(\sigma)}(\omega - \mathcal{L}_s)\hat{O}]. \quad (A3)$$

Here [cf. Eq. (4)]

$$c_\alpha^{(\sigma)}(\omega)\hat{O} = \sum [c_\alpha^\sigma(\omega)(\hat{d}^\sigma \hat{O}) - c_\alpha^{\bar{\sigma}*}(-\omega)(\hat{O}\hat{d}^\sigma)], \quad (A4)$$

with $c_\alpha^\sigma(\omega) \equiv \int_0^\infty dt e^{i\omega t} c_\alpha^\sigma(t)$. It is obtained as [46–48, 55]

$$c_\alpha^{(\pm)}(\omega) = \frac{1}{2} [\Gamma_\alpha^{(\pm)}(\mp\omega) + i\Lambda_\alpha^{(\pm)}(\mp\omega)], \quad (A5)$$

where $\Gamma_\alpha^\pm(\omega) = f_\alpha^\pm(\omega)\Gamma_\alpha(\omega)$ with $f_\alpha^+(\omega)$ the Fermi function of α -lead and $f_\alpha^-(\omega) = 1 - f_\alpha^+(\omega)$. In Eq. (A5), the real and the imaginary parts are the so-called bath interaction spectrum and *dispersion*, respectively [56]. They are related via the Kramers-Kronig relations,

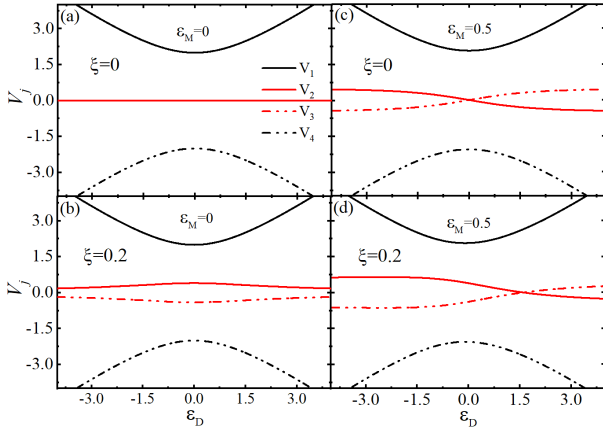


FIG. 7: (Color online) Low-energy spectrum characterizing the conductance peak positions (V_j) as a function of ε_D .

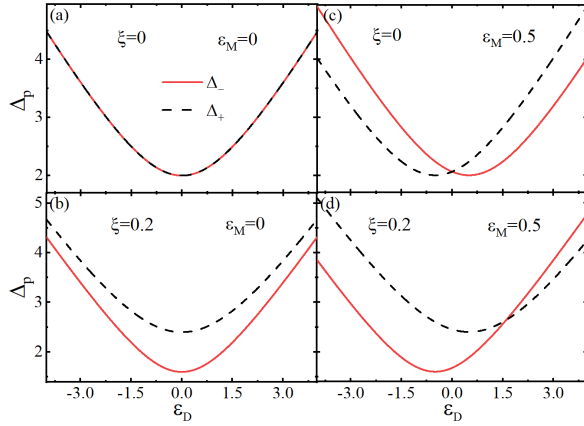


FIG. 8: (Color online) The parity-dependent Rabi frequency (Δ_p) as a function of ε_D .

$\Lambda_\alpha^{(\pm)}(\omega) = \mathcal{P} \int_{-\infty}^{\infty} \frac{d\omega'}{2\pi} \frac{1}{\omega \pm \omega'} \Gamma_\alpha^{(\pm)}(\omega')$. For the consideration of the Lorentzian-type form of the hybridization spectral density, i.e., $\Gamma_\alpha(\omega) = \frac{\Gamma_\alpha W_\alpha^2}{(\omega - \mu_\alpha)^2 + W_\alpha^2}$, with the coupling strength Γ_α and the bandwidth W_α of lead- α , one can obtain

$$\Lambda_\alpha^{(\pm)}(\omega) = \frac{\Gamma_\alpha(\omega)}{2\pi} \left\{ \text{Re} \left[\Psi \left(\frac{1}{2} + i \frac{\beta(\omega - \mu_\alpha)}{2\pi} \right) \right] - \Psi \left(\frac{1}{2} + \frac{\beta W_\alpha}{2\pi} \right) \mp \pi \frac{\omega - \mu_\alpha}{W_\alpha} \right\}, \quad (\text{A6})$$

where \mathcal{P} denotes the principle value of the integral, and $\Psi(x)$ is the digamma function.

Appendix B: Hamiltonian eigenspectrum

As well-known, the Majorana modes are related to the regular fermion through the transformation of $\gamma_1 = f + f^\dagger$ and $\gamma_2 = -i(f - f^\dagger)$. The system Hamiltonian of Eq. (2)

can be rewritten as

$$H_S = \varepsilon_D d^\dagger d + \varepsilon_M (f^\dagger f - \frac{1}{2}) + (\lambda_1 + \lambda_2) f^\dagger d + \text{H.c.}] + [(\lambda_1 - \lambda_2) f d + \text{H.c.}], \quad (\text{B1})$$

where the third and fourth terms corresponding to the normal tunneling and Andreev reflection processes, respectively. By introducing the occupation number operators $\hat{n}_D = d^\dagger d$ and $\hat{n}_M = f^\dagger f$, the Hamiltonian of Eq. (B1) can be expressed in the Fock basis, i.e., $\{|n_D n_M\rangle\}$, and becomes block diagonal in the odd-parity ($p = -1$) and even-parity ($p = +1$) subspaces. That is, the Hamiltonian of Eq. (B1) becomes

$$H_S = \begin{pmatrix} H_- & 0 \\ 0 & H_+ \end{pmatrix}, \quad (\text{B2})$$

where

$$H_- = \begin{pmatrix} \varepsilon_M & \lambda_1 + \lambda_2 \\ \lambda_1 + \lambda_2 & \varepsilon_D \end{pmatrix}. \quad (\text{B3a})$$

$$H_+ = \begin{pmatrix} 0 & \lambda_1 - \lambda_2 \\ \lambda_1 - \lambda_2 & \varepsilon_D + \varepsilon_M \end{pmatrix}, \quad (\text{B3b})$$

Apparently, there are intrinsic coherent Rabi oscillations in the odd and even parity subspaces induced by the normal tunneling and Andreev reflection processes, respectively. The corresponding parity-dependent Rabi frequency is given by Eq. (7). It is actually the energy difference between the two eigenstates of H_p ($|e_p\rangle$ and $|g_p\rangle$), i.e., $\Delta_p = \varepsilon_{e_p} - \varepsilon_{g_p}$. The corresponding eigenvalues are

$$\varepsilon_{e_+} = \frac{(\varepsilon_D + \varepsilon_M) + \Delta_+}{2}, \quad (\text{B4a})$$

$$\varepsilon_{g_+} = \frac{(\varepsilon_D + \varepsilon_M) - \Delta_+}{2}, \quad (\text{B4b})$$

for the even parity subspace, and

$$\varepsilon_{e_-} = \frac{(\varepsilon_D + \varepsilon_M) + \Delta_-}{2}, \quad (\text{B4c})$$

$$\varepsilon_{g_-} = \frac{(\varepsilon_D + \varepsilon_M) - \Delta_-}{2}, \quad (\text{B4d})$$

for the odd parity subspace.

The conductance peak positions in Eq. (8) comes from $V_1 = \varepsilon_{e_+} - \varepsilon_{g_-}$, $V_2 = \varepsilon_{g_+} - \varepsilon_{g_-}$, $V_3 = \varepsilon_{e_+} - \varepsilon_{e_-}$, and $V_4 = \varepsilon_{g_+} - \varepsilon_{e_-}$. They are closely related to the parity-dependent Rabi frequency (Δ_p) as can see Eq. (8). Both the peak positions and the Rabi frequencies can be tuned by the energy levels of the QD-wire system as displayed in Fig. 7 and Fig. 8, respectively. When $\varepsilon_M = 0$, the ZBP ($\Delta_+ = \Delta_-$) always occurs at any value of ε_D for MBSs ($\xi = 0$) and splits ($\Delta_+ \neq \Delta_-$) for ABSs ($0 < \xi < 1$) as depicted in Fig. 7 (Fig. 8) (a) and (b), respectively. Considering nonzero Majorana hybridization ($\varepsilon_M \neq 0$), the ZBP ($\Delta_+ = \Delta_-$) only occurs at $\varepsilon_D = 0$ for $\xi = 0$ and

again splits ($\Delta_+ \neq \Delta_-$) for $0 < \xi < 1$ as depicted in Fig. 7 (Fig. 8) (c) and (d), respectively. Moreover, the MBSs for finite ε_M (Fig. 7 (c)) displays that two central peaks at V_2 and V_3 have a crossing and becomes asymmetrical around $\varepsilon_D = 0$. The ABSs (Fig. 7 (d) and Fig. 8

(d)) however appears a ZBP ($\Delta_+ = \Delta_-$) at finite value of ε_D , which can be understood by Eq. (9). These features of peak positions are consistent with the demonstrations in Ref. 36.

-
- [1] A. Y. Kitaev, *Physics-Uspekhi* **44**, 131 (2001).
 [2] A. Kitaev, *Annals of Physics* **303**, 2 (2003).
 [3] C. Nayak, S. H. Simon, A. Stern, M. Freedman, and S. Das Sarma, *Rev. Mod. Phys.* **80**, 1083 (2008).
 [4] M. Leijnse and K. Flensberg, *Phys. Rev. Lett.* **107**, 210502 (2011).
 [5] R. M. Lutchyn, J. D. Sau, and S. Das Sarma, *Phys. Rev. Lett.* **105**, 077001 (2010).
 [6] Y. Oreg, G. Refael, and F. von Oppen, *Phys. Rev. Lett.* **105**, 177002 (2010).
 [7] K. Flensberg, *Phys. Rev. B* **82**, 180516 (2010).
 [8] S. Das Sarma, A. Nag, and J. D. Sau, *Phys. Rev. B* **94**, 035143 (2016).
 [9] C. Moore, T. D. Stanescu, and S. Tewari, *Phys. Rev. B* **97**, 165302 (2018).
 [10] K. T. Law, P. A. Lee, and T. K. Ng, *Phys. Rev. Lett.* **103**, 237001 (2009).
 [11] J. Danon et al., *Phys. Rev. Lett.* **124**, 036801 (2020).
 [12] G. C. Ménard et al., *Phys. Rev. Lett.* **124**, 036802 (2020).
 [13] V. Mourik et al., *Science* **336**, 1003 (2012).
 [14] M. T. Deng et al., *Nano Lett.* **12**, 6414 (2012).
 [15] A. Das et al., *Nat. Phys.* **8**, 887 (2012).
 [16] A. D. K. Finck, D. J. Van Harlingen, P. K. Mohseni, K. Jung, and X. Li, *Phys. Rev. Lett.* **110**, 126406 (2013).
 [17] S. M. Albrecht et al., *Nature* **531**, 206 (2016).
 [18] C.-X. Liu, J. D. Sau, T. D. Stanescu, and S. Das Sarma, *Phys. Rev. B* **96**, 075161 (2017).
 [19] O. A. Awoga, J. Cayao, and A. M. Black-Schaffer, *Phys. Rev. Lett.* **123**, 117001 (2019).
 [20] J. Avila, F. Penaranda, E. Prada, P. San-Jose, and R. Aguado, *Commun. Physics* **2**, 133 (2019).
 [21] P. San-Jose, J. Cayao, E. Prada, and R. Aguado, *Sci. Rep.* **6**, 21427 (2016).
 [22] J. Cayao, E. Prada, P. San-Jose, and R. Aguado, *Phys. Rev. B* **91**, 024514 (2015).
 [23] C. J. Bolech and E. Demler, *Phys. Rev. Lett.* **98**, 237002 (2007).
 [24] J. Nilsson, A. R. Akhmerov, and C. W. J. Beenakker, *Phys. Rev. Lett.* **101**, 120403 (2008).
 [25] L. Qin, W. Feng, and X.-Q. Li, *Chinese Physics B* **31**, 017402 (2022).
 [26] Y. Cao, P. Wang, G. Xiong, M. Gong, and X.-Q. Li, *Phys. Rev. B* **86**, 115311 (2012).
 [27] B. Zocher and B. Rosenow, *Phys. Rev. Lett.* **111**, 036802 (2013).
 [28] W. Feng, L. Qin, and X.-Q. Li, *New Journal of Physics* **23**, 123032 (2021).
 [29] D. E. Liu, M. Cheng, and R. M. Lutchyn, *Phys. Rev. B* **91**, 081405 (2015).
 [30] S. Smirnov, *New Journal of Physics* **19**, 063020 (2017).
 [31] G.-H. Feng and H.-H. Zhang, *Phys. Rev. B* **105**, 035148 (2022).
 [32] S. Smirnov, *Phys. Rev. B* **105**, 205430 (2022).
 [33] S. Smirnov, *Phys. Rev. B* **99**, 165427 (2019).
 [34] J. D. Sau, B. Swingle, and S. Tewari, *Phys. Rev. B* **92**, 020511 (2015).
 [35] M. Hell, K. Flensberg, and M. Leijnse, *Phys. Rev. B* **97**, 161401 (2018).
 [36] D. J. Clarke, *Phys. Rev. B* **96**, 201109 (2017).
 [37] E. Prada, R. Aguado, and P. San-Jose, *Phys. Rev. B* **96**, 085418 (2017).
 [38] M.-T. Deng et al., *Phys. Rev. B* **98**, 085125 (2018).
 [39] C.-X. Liu, J. D. Sau, and S. Das Sarma, *Phys. Rev. B* **97**, 214502 (2018).
 [40] A. Vuik, B. Nijholt, A. R. Akhmerov, and M. Wimmer, *SciPost Phys.* **7**, 61 (2019).
 [41] C.-K. Chiu and S. Das Sarma, *Phys. Rev. B* **99**, 035312 (2019).
 [42] C. Moore, C. Zeng, T. D. Stanescu, and S. Tewari, *Phys. Rev. B* **98**, 155314 (2018).
 [43] J. S. Jin, X. Q. Li, M. Luo, and Y. J. Yan, *J. Appl. Phys.* **109**, 053704 (2011).
 [44] Y. J. Yan and R. X. Xu, *Annu. Rev. Phys. Chem.* **56**, 187 (2005).
 [45] Y. Makhlin, G. Schön, and A. Shnirman, *Rev. Mod. Phys.* **73**, 357 (2001).
 [46] J. S. Jin, C. Karlewski, and M. Marthaler, *New J. Phys.* **18**, 083038 (2016).
 [47] P. Shi, M. Hu, Y. Ying, and J. Jin, *AIP ADVANCES* **6**, 095002 (2016).
 [48] Y. Xu, J. Jin, S. Wang, and Y. Yan, *Phys. Rev. E* **106**, 064130 (2022).
 [49] H.-A. Engel and D. Loss, *Phys. Rev. Lett.* **93**, 136602 (2004).
 [50] E. A. Rothstein, O. Entin-Wohlman, and A. Aharony, *Phys. Rev. B* **79**, 075307 (2009).
 [51] J. S. Jin, S. K. Wang, X. Zheng, and Y. J. Yan, *J. Chem. Phys.* **142**, 234108 (2015).
 [52] J. Y. Luo, X. Q. Li, and Y. J. Yan, *Phys. Rev. B* **76**, 085325 (2007).
 [53] B. Dong, X. L. Lei, and N. J. M. Horing, *J. Appl. Phys.* **104**, 033532 (2008).
 [54] D. Marcos, C. Emary, T. Brandes, and R. Aguado, *Phys. Rev. B* **83**, 125426 (2011).
 [55] J. S. Jin, J. Li, Y. Liu, X.-Q. Li, and Y. J. Yan, *J. Chem. Phys.* **140**, 244111 (2014).
 [56] R. X. Xu and Y. J. Yan, *J. Chem. Phys.* **116**, 9196 (2002).